Biochimica et Biophysica Acta 1807 (2011) 829–840

Contents lists available at ScienceDirect

Biochimica et Biophysica Acta

journal homepage: www.elsevier.com/locate/bbabio

The electronic structures of the S_2 states of the oxygen-evolving complexes of photosystem II in plants and cyanobacteria in the presence and absence of methanol

Ji-Hu Su [a,1], Nicholas Cox [a,*], William Ames [a,b], Dimitrios A. Pantazis [a,b], Leonid Rapatskiy [a], Thomas Lohmiller [a], Leonid V. Kulik [c], Pierre Dorlet [d], A. William Rutherford [d], Frank Neese [a,b], Alain Boussac [d], Wolfgang Lubitz [a,**], Johannes Messinger [e,***]

[a] Max-Planck-Institut für Bioanorganische Chemie, Stiftstrasse 34-36, D-45470 Mülheim an der Ruhr, Germany
[b] Lehrstuhl für Theoretische Chemie, Institut für Physikalische und Theoretische Chemie, Universität Bonn, Wegelerstr. 12, D-53115 Bonn, Germany
[c] Institute of Chemical Kinetics and Combustion, Institutskaya 3, 630090 Novosibirsk, Russia
[d] iBiTec-S, URA CNRS 2096, CEA Saclay, 91191 Gif-sur-Yvette, France
[e] Department of Chemistry, Chemical Biological Centre (KBC), Umeå University, S-90187 Umeå, Sweden

ARTICLE INFO

Article history:
Received 20 January 2011
Received in revised form 2 March 2011
Accepted 4 March 2011
Available online 13 March 2011

Keywords:
EPR
^{55}Mn-ENDOR
Photosystem II
OEC
Mn_4O_xCa cluster
Methanol
Orbach process
Raman process
Spin Hamiltonian

ABSTRACT

The electronic properties of the Mn_4O_xCa cluster in the S_2 state of the oxygen-evolving complex (OEC) were studied using X- and Q-band EPR and Q-band ^{55}Mn-ENDOR using photosystem II preparations isolated from the thermophilic cyanobacterium *T. elongatus* and higher plants (spinach). The data presented here show that there is very little difference between the two species. Specifically it is shown that: (i) only small changes are seen in the fitted isotropic hyperfine values, suggesting that there is no significant difference in the overall spin distribution (electronic coupling scheme) between the two species; (ii) the inferred fine-structure tensor of the only Mn^{III} ion in the cluster is of the same magnitude and geometry for both species types, suggesting that the Mn^{III} ion has the same coordination sphere in both sample preparations; and (iii) the data from both species are consistent with only one structural model available in the literature, namely the Siegbahn structure [Siegbahn, P. E. M. *Accounts Chem. Res.* **2009**, *42*, 1871–1880, Pantazis, D. A. et al., *Phys. Chem. Chem. Phys.* **2009**, *11*, 6788–6798]. These measurements were made in the presence of methanol because it confers favorable magnetic relaxation properties to the cluster that facilitate pulse-EPR techniques. In the absence of methanol the separation of the ground state and the first excited state of the spin system is smaller. For cyanobacteria this effect is minor but in plant PS II it leads to a break-down of the $S_T = ½$ spin model of the S_2 state. This suggests that the methanol–OEC interaction is species dependent. It is proposed that the effect of small organic solvents on the electronic structure of the cluster is to change the coupling between the outer Mn (Mn_A) and the other three Mn ions that form the trimeric part of the cluster (Mn_B, Mn_C, Mn_D), by perturbing the linking bis-μ-oxo bridge. The flexibility of this bridging unit is discussed with regard to the mechanism of O-O bond formation.

1. Introduction

In oxygenic photosynthesis, light-driven water-splitting is catalyzed by the oxygen-evolving complex (OEC) of photosystem II (PS II), a membrane-bound pigment–protein complex embedded in the thylakoid membranes of higher plants, green algae, and cyanobacteria. The OEC also comprises the protein matrix surrounding this inorganic core, and a nearby redox-active tyrosine residue (D_1-Y_{161}, Y_Z), for reviews see [1–10]. The latter mediates the proton-coupled electron transfer from the Mn_4O_xCa cluster to the photoactive reaction centre, P_{680}, a chlorophyll *a* species, which energetically drives water-splitting by undergoing sequential light-induced charge separation events. During water-oxidation, the Mn_4O_xCa cluster steps through a reaction cycle comprising five distinct redox intermediates [2,3,11].

Abbreviations: EPR, electron paramagnetic resonance; ENDOR, electron nuclear double resonance; ESEEM, electron spin-echo envelope modulation; PS II, photosystem II; OEC, oxygen-evolving complex; MeOH, methanol; CW, continuous wave; ZFS, zero-field splitting

* Corresponding author. N. Cox: Tel.: +49 208 306 3865.
** Corresponding author. W. Lubitz: Tel.: +49 208 306 3614.
*** Corresponding author. J. Messinger: Tel.: +49 90 7865933.
E-mail addresses: cox@mpi-muelheim.mpg.de (N. Cox), lubitz@mpi-muelheim.mpg.de (W. Lubitz), johannes.messinger@chem.umu.se (J. Messinger).
[1] Current address: Department of Modern Physics, University of Science and Technology of China, Hefei, Anhui 230026, China.

0005-2728/$ – see front matter © 2011 Elsevier B.V. All rights reserved.
doi:10.1016/j.bbabio.2011.03.002

These are known as the S_n states, where the index gives the number of stored oxidizing equivalents ($n=0$–4). Molecular oxygen is released during the $S_3 \rightarrow [S_4] \rightarrow S_0$ transition, with the S_4 state being a transient state that could so far not be trapped [12–16]. The S_1 state is stable in the dark. S_2 and S_3 are metastable intermediate states that can be studied after one or two flashes are given to a sample pre-incubated in the dark. S_0 is the most reduced state in the O_2-evolution cycle and can be produced by subjecting dark-adapted samples to three short flashes. In the dark, S_0 is slowly oxidized to S_1 by the nearby redox-active tyrosine residue Y_D^{ox} (D_2-Y_{161}) [17,18].

Single crystals of PS II from the thermophilic cyanobacterium *Thermosynechococcus elongatus* (*T. elongatus*) [19–23] have been intensively studied by X-ray diffraction and the geometric structure obtained is widely considered to be a model for PS II in all organisms. In spite of the advances in the X-ray structure analysis [22], the precise geometric structure of the OEC has yet to be determined, especially in the high redox states of the enzyme [24]. The inorganic core of the OEC consists of a Mn_4O_xCa cluster with $4 \leq x \leq 6$ indicating the number of oxygen bridges. As such, the current structural description of the Mn_4O_xCa cluster relies on a variety of spectroscopic techniques including: X-ray crystallographic data [21,23,25,26] and polarized EXAFS [10,27,28]. From this body of work, six types of computational structures have been developed as models for the OEC based on: i) London crystal structure [21,29–31]; ii) Berlin crystal structure [23,25,32–35]; iii) EXAFS core I [10,36]; iv) EXAFS core II [10,36]; v) EXAFS core III [10,36]; vi) Siegbahn model [4,37,38]. An in-depth review of these six structures is given in an earlier article [39].

It is well-established that the four Mn ions that constitute the OEC are magnetically coupled in all S_n states and that each S_n state ($n=0$–3) of the Mn_4O_xCa cluster has distinct EPR signals [6,40–50]. Of particular interest is the S_2 state which has a ground spin state of total spin $S_T=½$. This spin configuration gives rise to the well known S_2 state EPR multiline signal [40]. Depending on the conditions used the S_2 state of higher plant PS II also exhibits another broad EPR signal, centered at $g\sim4.1$ that has been assigned to an $S_T=5/2$ [51] spin state (see [52]). The $g\sim4.1$ signal can also be induced by near-infrared (NIR) illumination of the S_2 multiline state at temperatures ≤ 160 K [53]. In plant PS II, the presence of small alcohols prevents the formation of the $g\sim4.1$ signal. Amongst all the alcohols, methanol (MeOH) has a specific effect; it modifies the S_2 multiline signal and this signal is no longer sensitive to NIR illumination (discussed in [53–57]). The modified S_2 multiline signal is narrower than that seen for the non-treated plant PS II preparation, resolving fewer spectral lines. MeOH also has effects on the other S_n states. In spinach the S_0 state multiline signal can only be detected in the presence of MeOH [49,50,58]. In contrast, the parallel mode S_1 $g\sim4.9$ [45,46] and S_3 $g\sim8$ and $g\sim12$ EPR signals [59], and the EPR "split" signals, which arise from the weak magnetic interaction between the Mn_4O_xCa cluster and the Y_Z [60,61], are no longer visible when the MeOH concentration is increased to 3–5% (v/v). Curiously, in cyanobacterial PS II the addition of MeOH does not modify the S_2 multiline signal, the addition of MeOH does not prevent the formation of high spin S_2 states under NIR illumination[62] and the S_0 state multiline is observable also in the absence of MeOH [63].

Binding of small alcohols in close proximity to the Mn_4O_xCa cluster in PS II isolated from spinach was first demonstrated for the S_2 state by ESEEM spectroscopy by Force et al. [64,65] and later by Åhrling et al. [66]; however, the precise mode and site of binding was not resolved. In flash-induced oxygen evolution measurements it was recently observed that the miss parameter of PS II increases linearly with the MeOH concentration and that this effect is fully reversible up to 10% (v/v) MeOH [67]. This observation is consistent with MeOH binding at a substrate water binding site; however, other mechanisms may also explain this result.

The precise nature of the differences between the electronic structures of the Mn_4O_xCa cluster in plant and cyanobacterial PS II is not known to date. This is problematic, since for DFT calculations of the OEC often the geometric structure is derived based on X-ray diffraction measurements or (polarized) X-ray absorption measurements on *T. elongatus* samples, while electronic parameters such as the hyperfine couplings calculated for these structures are then compared to experimental EPR/ENDOR data obtained with PS II membranes from spinach [68–70]. Here we employ multi-frequency EPR and ^{55}Mn-ENDOR spectroscopy to gain detailed information about the species-dependent differences in the electronic structures of the S_2-states of the Mn_4O_xCa clusters of PS II isolated from higher plants (spinach) and cyanobacteria (*T. elongatus*).

2. Materials and methods

2.1. Sample preparation

PS II-enriched membranes from spinach (plant PS II) were prepared as described in [71]. These samples were concentrated to 20–30 mg Chl/ml in 3-mm Q-band EPR tubes by 30 min centrifugation at 4 °C. PS II core complexes (~30–40 μl) from *T. elongatus* were prepared as previously described [72–74]. The concentration of the EPR samples used was ~10 mg Chl/ml. The dark-adapted PS II samples poised in the S_1 state were illuminated by continuous white light at 200 K (dry ice/ethanol bath) for 3 min for plant PS II and 30 s for *T. elongatus* PS II.

2.2. Q-band pulse-EPR measurements

As in [69,75], Q-band pulse-EPR and ^{55}Mn Davies ENDOR measurements were performed at the indicated temperatures on a Bruker ELEXSYS E-580 Q-band pulse-EPR spectrometer equipped with a laboratory-built ENDOR cylindrical resonator and an Oxford-900 liquid helium cryostat and ITC-503 temperature controller, and with a SMT02 signal generator and an ENI 5100 L RF amplifier. Electron spin-echo (ESE)-detected field-swept spectra were measured with the pulse sequence of $\pi/2$-τ-π-τ echo, with $\pi=80$ ns and $\tau=440$ ns. The spin lattice relaxation time (T_1) was measured with the inversion recovery pulse sequence π-T-$\pi/2$-τ-π-τ echo, where $\pi=80$ ns, $\tau=400$ ns and T varies from 0.1 μs to 10 ms. ^{55}Mn Davies ENDOR measurements were collected by using SpecMan control software that varies the radiofrequency (RF) randomly in the desired range [75–77]. The employed pulse sequence was π-π_{RF}-T-$\pi/2$-τ-π-τ echo, where π, π_{RF}, T, and τ were 80 ns, 3.5 μs, 1.5 μs and 420 ns, respectively. A shot repetition time of 3 ms was used for all Q-band experiments with the exception of the T_1 measurements, where a shot repetition time of 5 ms was used.

3. Results

3.1. Species comparison

3.1.1. Q-band EPR/^{55}Mn-ENDOR experiments

ESE-detected EPR spectra of the Mn_4O_xCa cluster seen in PS II core complexes isolated from the cyanobacterium *T. elongatus* and higher plant spinach membranes, poised in the S_2 state are shown in Fig. 1a (black traces). A multiline signal is observed in both species [39,69,76], centered at approximately $g\sim2.0$ and spread over the same field range (1130–1320 mT). The signal from the stable tyrosyl radical, $Y_D^{\bullet}$, which appears as a strong, narrow (FWHM ~3 mT) signal centered at $g\sim2$ and obscures the central hyperfine lines of the S_2 state multiline signal, was removed for clarity of presentation. The hyperfine structure is very similar for both sample types; at least eight low-field lines (relative to the position of the $Y_D^{\bullet}$ radical) and 10 high field lines are observed for both sample types.

Differences between the two species are more readily observed using ^{55}Mn-ENDOR. Fig. 1b shows the ^{55}Mn-ENDOR signals seen for

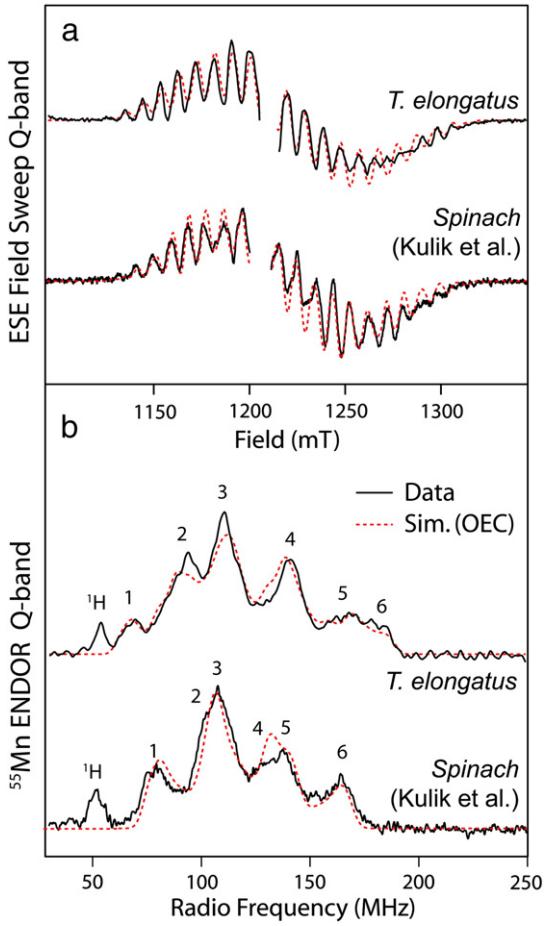

Fig. 1. EPR/ENDOR spectra of PS II core complexes obtained from *T. elongatus* PS II and PS II-enriched membranes from spinach, poised in the S_2 state with 4% MeOH added (solid black lines). (a) Q-band pulse ESE-detected field sweep. The derivative spectra represent the pseudo modulated (2 mT) raw data. The $Y_D^{\bullet}$ signal centered about g~2 was removed for clarity of presentation. The small offset between the two multiline spectra is caused by the fact that each spectrum was recorded at a slightly different microwave frequency. Experimental parameters: microwave frequencies: 33.69 GHz (*T. elongatus*), 33.85 GHz (spinach); shot repetition rate: 5 ms; microwave pulse length (π): 80 ns, τ: 440 ns, temperature: 4.2 K. (b) Q-band pulse ^{55}Mn-Davies ENDOR. The *T. elongatus* spectrum presented was smoothed using a 5 point moving average. Experimental parameters: microwave frequencies: 34.05 GHz (*T. elongatus*), 33.85 GHz (spinach); magnetic field: $B_0 = 1260$ mT; shot repetition rate: 5 ms; microwave pulse length (π): 80 ns, τ: 440 ns, RF pulse (π_{RF}): 3.5 μs. The red dashed lines superimposing each trace represent the least squares fittings to the whole data sets of each species using a model based on the Spin Hamiltonian formalism [39,69]. The optimized parameter sets are given in Table 1.

the *T. elongatus* and spinach PS II preparations described above, poised in the S_2 state, and measured at $B_0 = 1260$ mT. The spinach and *T. elongatus* preparations give rise to comparable but not identical ^{55}Mn-ENDOR spectra. The total spectral breath of the ^{55}Mn-ENDOR spectrum is significantly larger in *T. elongatus* as compared to spinach [69,75]. The high frequency edge shifts 20 MHz to higher frequency and the low frequency edge decreases by approximately the same degree. The lowest field peak, centered at ~52 MHz, originates from the magnetic coupling of protons with the Mn_4O_xCa cluster. Approximately six peaks are observed for the OEC of *T. elongatus*. This is in contrast to spinach PS II, where only four peaks are clearly visible; peaks 2 and 4 appear as shoulders on peak 3 and 5, respectively. It is noted that the above described line shapes of the ^{55}Mn-ENDOR signals of both sample types are essentially invariant over the 1190–1260 mT magnetic field range, consistent with their assignment to the OEC [69,76].

3.1.2. Spectral simulations

The S_2-state Q-band EPR and Q-band pulse ^{55}Mn ENDOR spectra were simulated using the Spin Hamiltonian formalism described in [69,76,78]. Here, the S_2 multiline signal is considered to arise from an effective $S = ½$ ground state, coupled to four ^{55}Mn nuclei. The hyperfine interaction was treated with second-order perturbation theory. The quadrupole interaction was not explicitly considered; it was assumed to contribute to the fitted line-width (for details on the simulation procedure see [39,69]).

The fitted $\boldsymbol{G}$ and hyperfine tensors are given in Table 1. Four hyperfine tensors are required to fit the absorption and 1st derivative line shapes and ENDOR spectra for both sample types (Fig. 1a and b, red dashed line). Near-axial symmetry was seen for the fitted hyperfine tensors for both species. With the exception of $\boldsymbol{A}_1$, the z (parallel) component of all hyperfine tensors was the largest. Comparison of the fitted parameters obtained for spectra from spinach and *T. elongatus* demonstrates that there are only subtle differences between the two species. Importantly, the four isotropic values ($A_{i,\mathrm{iso}}$) of the fitted hyperfine tensors (Table 1) all approximately match both OECs suggesting that there is no significant change in the electronic structure/coupling scheme i.e. a difference of less than <10% is seen between the fitted $A_{i,\mathrm{iso}}$ values. The isotropic components of three of the hyperfine tensors are close to that observed for monomeric Mn^{III}/Mn^{IV} complexes, while that of the fourth Mn is ~1.5 times larger than that reported in the current literature [70,79–82]. This suggests that all four Mn ions equally contribute to the EPR and ENDOR spectra.

The reason for the increase in breadth of the S_2 state ^{55}Mn-ENDOR spectrum of *T. elongatus* as compared to spinach is due to a small increase in hyperfine tensor anisotropy (A_{aniso}). This is seen particularly for hyperfine tensors $\boldsymbol{A}_1$ and $\boldsymbol{A}_4$, which define the high- and low-field edges of the ENDOR spectrum, respectively. The ENDOR signals associated with these two Mn ions are spread over a larger frequency range leading to a broadening of the entire signal envelope. Consistent with this description is the apparent decrease in signal intensity of the edges relative to the intense central line (peak 3) of the ^{55}Mn-ENDOR spectrum of *T. elongatus* as compared to spinach.

3.2. The effect of methanol

3.2.1. T_1 relaxation

Over a 5–10 K temperature range, two phonon relaxation processes usually form the dominant T_1 relaxation pathway for metallocofactors seen in enzymes, namely the Raman and Orbach processes

Table 1
The principal values of the effective $\boldsymbol{G}$ and ^{55}Mn hyperfine tensors for the simulations of the S_2 spectra of *T. elongatus* and spinach PS II.

		$\boldsymbol{G}$	$\boldsymbol{A_i}$ (MHz)			
			$\boldsymbol{A_1}$	$\boldsymbol{A_2}$	$\boldsymbol{A_3}$	$\boldsymbol{A_4}$
T. elongatus	x	1.971	350	249	202	148
	y	1.948	310	227	182	162
	⊥	1.960	330	238	192	155
	z (‖)	1.985	275	278	240	263
	iso	1.968	312	251	208	191
	aniso	0.025	55	-40	-48	-108
Spinach	x	1.997	310	235	185	170
	y	1.970	310	235	185	170
	⊥	1.984	310	235	185	170
	z (‖)	1.965	275	275	245	240
	iso	1.977	298	248	205	193
	aniso	0.019	35	-40	-60	-70

The isotropic G_{iso} and $A_{i,\mathrm{iso}}$ ($i = 1$–4) values are the average of the individual values: $G_{\mathrm{iso}} = (G_x + G_y + G_z)/3$ and $A_{i,\mathrm{iso}} = (A_{i,x} + A_{i,y} + A_{i,z})/3$. The equatorial and axial G and $\boldsymbol{A}_i$ values are defined as: $G_\perp = (G_x + G_y)/2$, $G_\parallel = G_z$ and $A_{i\perp} = (A_{i,x} + A_{i,y})/2$, $A_{i,\parallel} = A_{i,z}$. The anisotropy in the G and $\boldsymbol{A}_i$ values is expressed as the difference between the perpendicular and parallel components of the tensor.

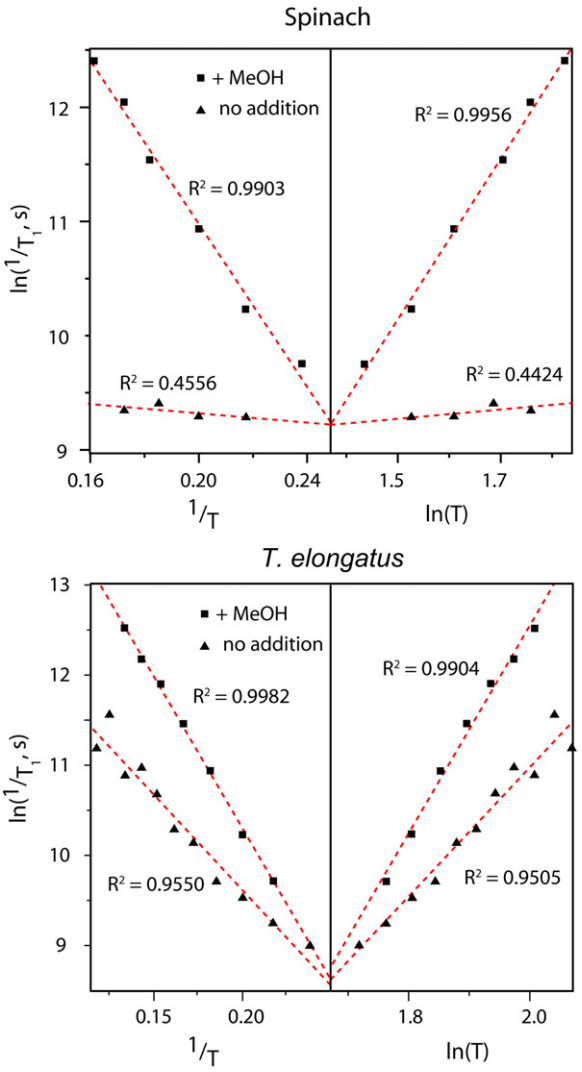

Fig. 2. The temperature dependence of the T_1 relaxation time of the OEC poised in the S_2 multiline state in PS II samples containing 4% MeOH (■) and in the absence of MeOH (no addition) (▲). The left hand side panel data plots the inverse temperature vs. the natural logarithm of the inverse of the T_1 time (Orbach process). The right hand panel plots the natural logarithm of the inverse temperature vs. the natural logarithm of the inverse of the T_1 time (Raman process). Electron spin-echo-detected T_1 relaxation data were measured using a 3 pulse sequence: π-T-$\pi/2$-τ-π-τ echo, using $\pi = 80$ ns, $\tau = 440$ ns, and T was swept over the range of 0.1–10 ms. An estimate of the T_1 time was made by fitting the raw data to a bi-exponential decay collected at each temperature. The superimposed red lines correspond to a linear fit of the data. Experiments were performed at $B_0 = 1260$ mT.

[83,84]. Both processes rely on the system containing spin levels that are thermally accessible, but each has a slightly different dependence on the measurement temperature (T):

$$\ln\left(\frac{1}{T_1}\right) = \frac{\Delta}{T} \quad (1)$$

$$\ln\left(\frac{1}{T_1}\right) \propto \ln(T) \quad (2)$$

It is noted that the relaxation rate of an Orbach process is dependent on the ground to first excited state energy separation (Δ). As such, an estimate of the energy ladder can be made when this process is the dominant relaxation process [83,84]. Previous studies in spinach PS II [85] in the presence of a small percentage of MeOH, demonstrated that the OEC cluster in the S_2 multiline state displays dominantly

Table 2
The energy separation Δ between the ground and first excited electronic states for the S_2-state in plant PS II and *T. elongatus* PS II samples assuming an Orbach relaxation process.

		Δ (cm^{-1})	
		No addition	+ MeOH
T. elongatus	T_1 relaxation	13.5 ± 1.2	22.4 ± 0.6
Spinach	T_1 relaxation	2.7 ± 0.5	24.7 ± 1.2, 36.5 [85]
	CW EPR	~6 [48,54]	12 [48,54], 30 [48,54]

an Orbach relaxation over the 5–10 K temperature range. This work reported a ground to first excited state energy difference (Δ) of 35 cm^{-1} for the S_2 state [85]. We have repeated this experiment using our plant PS II membrane samples and found that over the 4.6—7.5 K temperature range both the relationships $\ln(1/T_1)$ versus $1/T$ and $\ln(1/T_1)$ vs. $\ln(T)$ are approximately linear ($R^2 = 0.9903$ and $R^2 = 0.9956$, respectively; Fig. 2, upper panel). Thus, under our experimental conditions, we cannot distinguish whether an Orbach or Raman relaxation process dominates. If an Orbach process is assumed, Δ is estimated to 24.7 ± 1.2 cm^{-1} (Table 2). This value is lower than that seen in the earlier study of Lorigan and Britt [85], but still of approximately the same magnitude. In the absence of MeOH, the behavior of the T_1 time changes dramatically. The observed spin-echo is more difficult to measure in samples without MeOH (no addition) and as such the data quality is poorer. Nevertheless, a semi-quantitative description of the system can still be made. As before, the data are equally consistent with either an Orbach or a Raman process. If we again assume an Orbach process, the energy difference (Δ) has collapsed to 2.7 ± 0.5 cm^{-1} (Table 2). This value is small and should be considered as a lower bound for Δ. A decrease in the observed Δ is consistent with literature CW EPR results. In higher plant spinach a Δ of ~6 cm^{-1} was measured for the non-MeOH treated OEC S_2 multiline state [48] as opposed to ~25–35 cm^{-1} when MeOH is present. Similar results have been observed for OEC poised in the S_1-state. A ground to first excited state energy separation of $\Delta = 1.7$ cm^{-1} was reported for higher plant spinach in the absence of solvents poised in the S_1 state [46]. These results were obtained by examining the temperature dependence of the S_1 parallel polarization CW EPR signal. This signal arises from a low lying excited spin state ($S = 1$). It was observed that the excited state signal was lost by the addition of MeOH. That is to say, the proportion of S_1 in the EPR visible excited state ($S = 1$) decreased and that in the diamagnetic $S = 0$ ground state increased upon MeOH addition which suggests that Δ increased by at least ~7 cm^{-1}, see [46].

Analogous results are observed for *T. elongatus* (Fig. 2, lower panel) Unlike the spinach PS II data presented above, our results for the MeOH treated OEC poised in the S_2 state in *T. elongatus* do slightly favor an Orbach process (R^2 of 0.9982 vs. 0.9904 for Raman process). The Orbach fit gave a Δ of 22.4 ± 0.6 cm^{-1} approximately that seen in our spinach measurements. The temperature dependence of T_1 was measured at several field positions yielding values within the error stated. In contrast to spinach samples, similar T_1 times are observed in *T. elongatus* preparations with and without MeOH. The *T. elongatus* preparation without MeOH was consistent with either Orbach (R^2 of 0.9550) or Raman (R^2 of 0.9505) relaxation. If Orbach relaxation is assumed, the energy difference between the ground and first excited state Δ is estimated to be 13.5 ± 1.2 cm^{-1} (Table 2).

3.2.2. CW EPR and ^{55}Mn-ENDOR

The effect of small alcohols on the CW EPR line shape of the S_2 multiline signal of higher plants has been well documented [53–57]. A slight narrowing of the S_2 multiline spectrum is observed when MeOH is added (Fig. 3a). The amplitudes of the central lines of the multiline pattern increase to the detriment of the external lines and the super hyperfine structure is lost. The corresponding ^{55}Mn-ENDOR spectrum (Fig. 3b) also changes. In samples to which MeOH is not added the

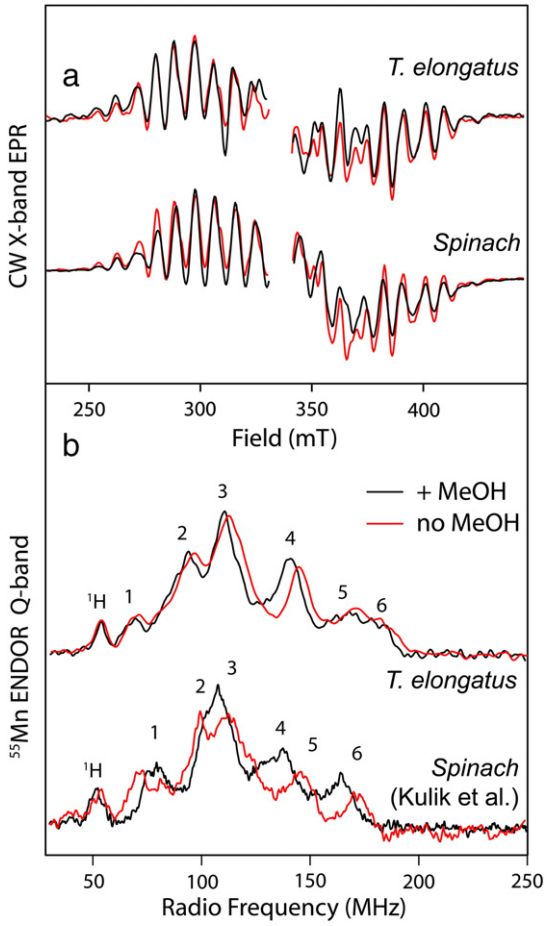

Fig. 3. The effect of MeOH on the EPR/ENDOR spectra of PS II core complexes obtained from *T. elongatus* and spinach BBY membranes, poised in the S_2 state. Solid black lines: 4% MeOH; red lines: in the absence of MeOH. (a) *CW* X-band EPR. The $Y_D^{\bullet}$ centered about g~2, was removed for clarity of presentation. Experimental parameters: microwave frequencies: 9.4 GHz; microwave power: 20 mW; modulation amplitude: 25 G; time constant: 80 ms, temperature: 8.6 K. (b) Q-band pulse ^{55}Mn-Davies ENDOR. The *T. elongatus* spectrum presented was smoothed using a 5 point moving average. Experimental parameters: microwave frequencies: 34.05 GHz (*T. elongatus*), 33.85 GHz (spinach); magnetic field: $B_0 = 1260$ mT; shot repetition rate: 5 ms; microwave pulse length (π): 80 ns, τ: 440 ns, RF pulse (π_{RF}): 3.5 μs.

^{55}Mn ENDOR spectrum is broader and more structured (~115 MHz width) spanning 65−180 MHz [69,76]. The same behavior is not observed for *T. elongatus*. The addition of MeOH does not alter the CW EPR line shape of the S_2 multiline signal. Consistent with this earlier result, it is observed that the ^{55}Mn ENDOR spectrum also does not change significantly when MeOH is added to the sample. Only subtle changes are observed in the positions of peaks 4 and 6, both shifting to slightly lower radio-frequencies when MeOH is added. The *T. elongatus* spectra shown in Fig. 3 are similar to those reported in a previous study of Pudollek et al. [108]; the total ENDOR signal spans approximately the same width but there are differences in the intensities of the individual lines.

4. Discussion

4.1. General remarks

Refined crystal structure models obtained from thermophilic cyanobacteria form the basis for all current models of the OEC. However much of the spectroscopic data in the literature were obtained using PS II from plants rather than *T. elongatus*. As mentioned in the introduction, although the PS II from the two species behave similarly, some differences are observed. The results presented here demonstrate that the OEC of the two species are highly similar but not identical. The small differences that are observed are interpreted within a framework in which the spin manifold/energy ladder of the higher plant system is intrinsically more variable than the cyanobacterial system, with the former being more strongly affected by the addition of MeOH. The difference between the action of MeOH in the two species can be explained in two alternative ways. (i) Solvent access to the Mn cluster in the plant vs. cyanobacterial OEC may be different such that MeOH is unable to directly interact with the OEC in the *T. elongatus*. Earlier ESEEM measurements have already shown that MeOH binds to the plant OEC [64,66]. This may reflect changes close to the active site or properties of the more peripheral subunits (which are known to be different between plants and cyanobacteria) and related channels [21,25,86,87]. (ii) Alternatively, the nature of the interaction between MeOH and OEC (e.g. its binding site, the type of binding, or the result of its binding) must somehow differ in the two species. We consider the latter option more reasonable. The change in the electronic structure, as inferred from T_1 relaxation measurements when MeOH is added is similar (an increase in Δ) and only differs by a factor of two in magnitude for both species (~10 cm^{-1} for *T. elongatus* vs. 20 cm^{-1} for spinach). As such, the work presented here suggests that some degree of flexibility can be accommodated within the 1st or 2nd coordination sphere of the Mn_4O_xCa cluster without impairing water-splitting function. This is in line with a number of mutant studies that show that several mutations in the first coordination sphere do not impair water-splitting [88] or the shape of the S_2 multiline signal [89].

4.2. OEC models consistent with higher plant spinach EPR/ENDOR data

In an earlier article [39] we examined the effect of Ca^{2+}/Sr^{2+} substitution on the X- and Q-band EPR and Q-band ^{55}Mn-ENDOR spectra of the S_2 multiline signal of *T. elongatus* (with MeOH). These results were then used to discriminate between current literature models of the OEC. As stated in the introduction, there are currently six types of DFT models for the OEC. Of those for which we had the coordinates at the time of the study, we demonstrated that only one coupling scheme, based on the Siegbahn core [4,37,38], is consistent with all EPR/ENDOR data. It is noted that the Siegbahn structure in our study was slightly modified (as compared to the structure reported in [4]) to confer it a ground state of spin $S_T = ½$, see Pantazis et al. [36]. This model was selected as it: (i) reproduces the correct ground state spin multiplicity ($S_T = ½$); (ii) the correct ground to first excited state energy difference (to within a factor of 2–3); (iii) yields a spin projection coefficient of $|\rho| \sim 1$ for all four Mn ions, consistent with the EPR/ENDOR data; and (iv) gave reasonable estimates for the on-site zero-field splitting (ZFS) of the Mn^{III} i.e. within the range seen for model complexes and the zero-field splitting was affected by Sr^{2+} substitution in a way that is consistent with the changes seen in polarized EXAFS and DFT calculations.

It does not immediately follow that the Siegbahn model is also consistent for the higher plant spinach S_2 state (with MeOH); this must be tested. It is noted that criteria (i), (ii) and (iii) apply equally well to both the S_2 states of spinach and *T. elongatus*. Both require the ground state to be $S_T = ½$, spin projection coefficients for all four Mn of approximately 1 and a similar ground to first excited state energy difference, in MeOH treated samples. The only question that remains is whether the Siegbahn model also gives sensible estimates for the on-site ZFS (d) of the Mn^{III} for the spinach OEC (criterion iv). As d is reflected by the fitted hyperfine anisotropy, which is shown above to change between higher plant spinach and *T. elongatus* (see Table 1), its contribution to the energy levels of the system for the two species must differ.

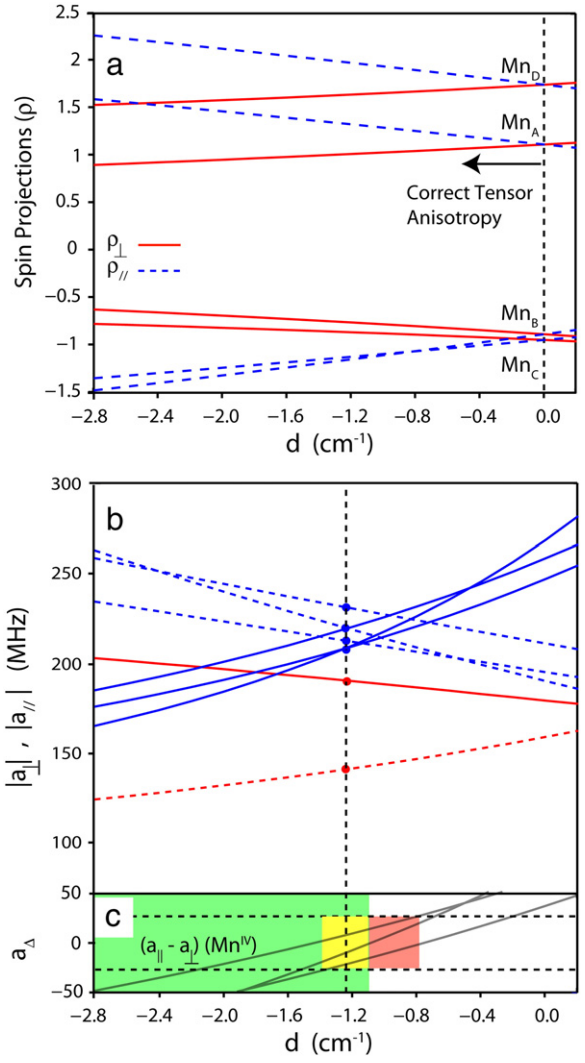

Fig. 4. (a) The dependence of the spin projection factors ($\rho_\perp$, $\rho_\parallel$) on the zero-field splitting parameter (d) of the Mn^{III} ion assuming the exchange coupling model for the Siegbahn core (scheme Fig. 5A). (b) The dependence of the on-site hyperfine tensor components ($a_\perp$, $a_\parallel$) of the spinach Mn_4O_xCa cluster in the presence of methanol for each of the four manganese ions on the zero-field splitting parameter (d) of the Mn^{III} ion. The bottom panel (c) shows the difference (a_Δ) between the parallel ($a_\parallel$) and perpendicular ($a_\perp$) hyperfine components of the three Mn^{IV} ions. The green shaded region represents the range of ZFS values for the Mn^{III} seen in model complexes (when $d<0$). The red shaded region represents the range of acceptable ZFS values for the Mn^{III} which are consistent with the electronic coupling model, i.e. the range over which the intrinsic hyperfine anisotropy of the Mn^{IV} ions is within the range seen for model complexes. The intersection of the green and red regions is shown by the yellow shaded region. Table 3 lists the intrinsic hyperfine tensor components for all four Mn ions calculated at the midpoint of the range of consistent d values, i.e. the midpoint of the yellow shaded region.

A description of how the on-site ZFS of the Mn^{III} can be estimated from fitted effective Spin Hamiltonian parameters (i.e. A_1, A_2, A_3, A_4) can be found in an earlier article [39]. A brief summary is given below. The effect of the on-site ZFS of the Mn^{III} ion can be taken into account in the calculation of the spin projection coefficients. The spin projection coefficients provide a means to scale the effective Spin Hamiltonian parameters to the on-site (intrinsic) parameters of the individual Mn ions. It is the on-site (intrinsic) parameters that can be compared to literature values. The inclusion of the on-site ZFS of the Mn^{III} requires that the spin projections for all four Mn ions must be considered as tensors as opposed to scalar quantities; that is to say that their magnitude is now orientationally dependent. Fig. 4a displays the dependence of the parallel and perpendicular components of the spin projection tensor of each of the four Mn ions (A, B, C, D) as a function of the ZFS of the Mn^{III} ion. When $d=0$, the two components are necessarily equal. It can be readily observed that the correct anisotropy of the effective hyperfine tensors of the Mn^{IV} ions can only be reproduced if the d value is negative. This yields a larger parallel as opposed to perpendicular spin projection component, as seen for the effective Mn^{IV} hyperfine tensors (A_2-A_4). The on-site/intrinsic parallel and perpendicular hyperfine tensor components ($a_\parallel$, $a_\perp$;) can then be calculated from the ratio of the fitted effective hyperfine tensor components ($A_\parallel$, $A_\perp$) and the spin projection components seen in panel a ($\rho_\parallel$, $\rho_\perp$). Their dependence on the choice of d is shown in Fig. 4b. An estimate for the ZFS of the Mn^{III} ion can be made using panel c. It shows the anisotropy of the three Mn^{IV} ions i.e. the difference between $a_\parallel$, $a_\perp$, shown in panel b. It is expected that the intrinsic anisotropy of the three Mn^{IV} ions is small, less than 30 MHz (for a full discussion see Cox et al. [39]). The values of d that are consistent with this range are shown by the red shaded region. Literature values for d as measured in monomeric Mn^{III} model complexes provide a second constraint. This range is shown by the green shaded region. The intersection of the red and green shaded regions, colored yellow, then gives the allowed range of d for the Mn^{III} of the OEC. The on-site hyperfine parameters for all four Mn ions calculated at the midpoint of this acceptable range are given in Table 3.

The inferred on-site ZFS of the Mn^{III} ion for the plant OEC is $\sim -1.2\ cm^{-1}$ (see Fig. 4, caption). A d value of $-1.2\ cm^{-1}$ is small for a Mn^{III} ion, falling just inside the range of d values seen in model complexes i.e. $1<|d|<5\ cm^{-1}$, see [39]. The d value is negative and the intrinsic parameters for the Mn^{III} are: $a_{iso}\sim 174$ MHz, $a_\perp\sim 190$ MHz, $a_\parallel\sim 141$ MHz, a_{aniso} −49 MHz. These values are consistent with a Mn^{III} ion with a 5 coordinate square-pyramidal or 6 coordinate tetragonally elongated ligand field. These are approximately the same values as determined for the *T. elongatus* (see Table 3 and [39]). Importantly, the inferred geometry of the Mn^{III} is consistent with the Siegbahn model; the Mn^{III} in the Siegbahn structure has a square-pyramidal ligand field. Thus, this model is consistent with the EPR/ENDOR data for the S_2 states of both *T. elongatus* and spinach. We note that the small difference inferred between the d values for the *T. elongatus* and spinach PS II may be real or an indirect consequence of the above

Table 3
Calculated spin projection tensor components ($\rho_\perp$, $\rho_\parallel$) and hyperfine tensor components ($a_\perp$, $a_\parallel$) for the 4 Mn ions of PS II in the S_2 state.

		$\rho_\perp$	$\rho_\parallel$	$a_\perp$	$a_\parallel$	a_{iso}	a_{aniso}
T. elongatus	Mn_A (Mn^{IV})	1.01	1.33	235.2	209.6	226.6	−25.6 (−8.5)
d (Mn^{III}) = −1.32 to −1.26 cm^{-1}	Mn_B (Mn^{IV})	−0.77	−1.16	201.7	226.7	210.0	25.0 (8.3)
d_{midpt} = −1.29 cm^{-1}	Mn_C (Mn^{IV})	−0.87	−1.12	221.6	213.5	218.9	−8.0 (−2.7)
	Mn_D (Mn^{III})	1.62	1.96	203.3	140.5	182.4	−62.8 (−20.9)
Spinach	Mn_A (Mn^{IV})	1.02	1.32	231.0	209.1	223.7	−21.9 (−7.3)
d (Mn^{III}) = −1.34 to −1.1 cm^{-1}	Mn_B (Mn^{IV})	−0.77	−1.15	219.0	209.4	216.1	−10.0 (−3.3)
d_{midpt} = −1.22 cm^{-1}	Mn_C (Mn^{IV})	−0.87	−1.11	212.5	219.9	224.9	7.4 (2.4)
	Mn_D (Mn^{III})	1.62	1.95	190.4	141.3	174.0	−49.0 (−16.3)

The isotropic a_i values are defined as: $a_{i,iso}=(2a_{i\perp}+a_{i\parallel})/3$. The anisotropy $a_{i,aniso}$ is expressed as the difference between the parallel and perpendicular component of the tensor. For direct comparison to the work of Peloquin et al. [70] the anisotropy is also expressed as the difference divided by three (see value in brackets).

described, small changes in the electronic structure of the Mn_4O_xCa cluster i.e. as the Δ is slightly different for plant and *T. elongatus* samples with MeOH, their electronic structure (exchange coupling topology) must be slightly different. The important result is that the *d* value is similar for the two species and consistent with literature benchmarks (see [39], supporting information Table S3). The Siegbahn model as presented here is in agreement with the experimental results of Teutloff et al. [109]. These authors performed an EPR/ENDOR study on PS II single crystals. The comparison of these results to the crystal structure of Guskov et al. [22], allowed a tentative assignment of the position of the Mn^{III}. Its preferred location was within bonding distance to the Asp342 residue. Here it was assumed that the Mn-Asp342 bond defines the Jahn-Teller axis of the Mn^{III} ion.

4.3. Decoupling of the OEC

A uniquely determined experimental solution for the ladder of spin states of the Mn_4O_xCa cluster can not be obtained. If only pairwise interactions are considered between the four Mn ions, six exchange couplings are required to describe the energy ladder of the system. Experimentally though, only one observable is measured, the ground to the first excited state energy-level difference (Δ). As a consequence, a simpler model is often invoked for interpreting EPR data, in which the energy levels of the system are described in terms of an effective coupling constant, J_{eff} ($\Delta = 3/2J_{eff}$, for the S_2 multiline). Here, the four-spin system is described in terms of a two-spin system as shown in Fig. 5b and c, respectively. The electronic coupling component of the Spin Hamiltonian for this simplified system takes the form:

$$H = -J_{eff} S_1 \cdot S_2 \tag{3}$$

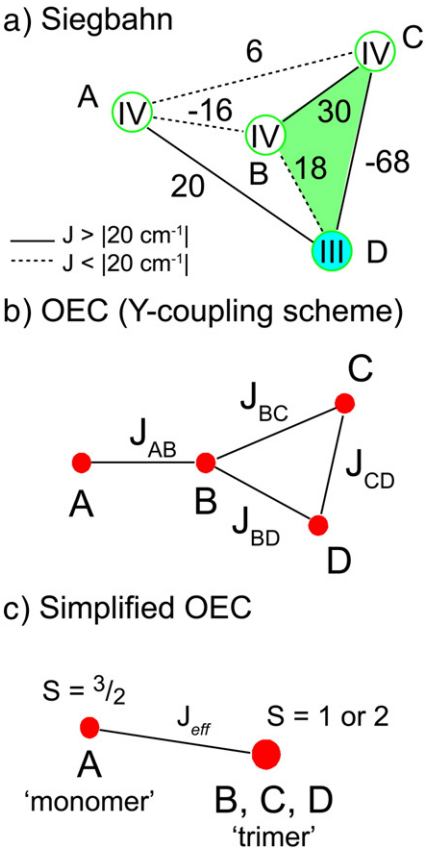

Fig. 5. Current models for the electronic structure of the OEC. (a) The J coupling scheme for the Siegbahn structure [4,36]; (b) Y-coupling scheme developed from EPR/ENDOR [69]; (c) a simplified OEC coupling scheme in which the Y-scheme is approximated by two spins.

where S_1 and S_2 describe the two fragments of the tetramer: a monomeric Mn^{IV} ($S = 3/2$) and a coupled trimer $(Mn^{IV})_2Mn^{III}$ of total spin $S = 1$ or 2, and J_{eff}, the coupling between them [40]. The spin state ladder for this system is $E_s = J_{eff}/2S(S+1)$. Within this simple model, solvent-induced effects are easily rationalized. MeOH somehow modulates the electronic coupling of the monomeric Mn to the trimer (i.e. *J*). MeOH binding causes *J* to increase by approximately 4- to 10-fold in spinach and ~2 fold for *T. elongatus* in the S_2 state.

It is useful to consider how the simple model described above maps onto the Siegbahn model (Fig. 5a). The Siegbahn model broadly fits with the Y-coupling scheme topology [36,39] (Fig. 5b), which was developed on the basis of (3 + 1) coupling schemes first proposed by Peloquin et al. [70] . Mn_B, Mn_C and Mn_D couple together to form the trimer fragment with a total ground state spin of $S = 1$. To this fragment the Mn_A monomer fragment is coupled. The effective coupling J_{eff} in the simple model above includes contributions from the J_{AB}, J_{AC}, J_{AD} exchange pathways. In the work of Pantazis et al. [36] it was noted that the ground to first excited state energy difference in this model was dependent on the magnitude of the coupling between Mn_A and the trimer unit and that the net sign of this interaction also defined the spin multiplicity of the ground state. Thus, even within this more complicated electronic coupling scheme, a mechanism seems reasonable in which solvents such as MeOH modulate the electronic coupling of the monomeric Mn to the trimer.

This simple description of the action of small organic solvent molecules on the electronic structure of the OEC also provides a rationale for the changes observed in the width and line shape of both the EPR and ENDOR data. The line shape of the EPR and ENDOR spectra changes because the contribution of the on-site ZFS of the Mn^{III} changes. This is because the relative contribution of the on-site ZFS of the Mn^{III} ion to the energy levels of the cluster is dependent on Δ. For large Δ, the on-site ZFS can be considered a small perturbation of the electronic structure. Within this regime, variation in Δ should not significantly change the spin projection coefficients; the perpendicular and parallel components ($\rho_\perp$, $\rho_{||}$) of the spin projection tensor are approximately equal. If however Δ is of the same size as the on-site ZFS of the Mn^{III}, relatively small changes in Δ can lead to large changes in the spin projection coefficients and thus large changes in the effective hyperfine tensors. For the OEC, Δ is small, being at most an order of magnitude larger than the on-site ZFS of the Mn^{III} and thus the second regime holds (Fig. 6).

It was shown above that in plant PS II, there is a large change of Δ induced by MeOH. This should then lead to a large change in the spin projection coefficients of the OEC and as a consequence, a large change in the effective hyperfine tensors. Compared to the MeOH treated system (the system that was simulated), it is expected that in the absence of MeOH the perpendicular and parallel components ($A_\perp$, $A_{||}$) of the effective hyperfine tensors should diverge, leading to an increase in the width of both the EPR and ^{55}Mn-ENDOR spectrum. This is exactly what is observed experimentally. Similarly, as the MeOH-induced change in Δ is much smaller in the cyanobacteria, no large change in the spin projection coefficients is expected and thus no change should be seen in the EPR and ENDOR spectra.

It can be shown that the Siegbahn model is at least semi-quantitatively consistent with the mechanism described above. This is shown in Fig. 7. Here the coupling between Mn_A and the trimer is varied to demonstrate how the energy gap and spin projections change as a function of this coupling. The coupling is varied in a simple way; the three exchange couplings that connect Mn_A to the trimer (J_{AB}, J_{AC}, J_{AD}) are simply multiplied by a factor *c*. As such, the factor *c* represents an average increase/decrease in the connectivity of the two OEC fragments, the $S = 3/2$ (Mn_A) and the $S = 1$ (Mn_B, Mn_C, Mn_D). The on-site ZFS of the Mn^{III} was fixed to the value determined in section 4.2, i.e. $d = -1.2\ cm^{-1}$. As expected, over the range of energy gap values determined for *T. elongatus* ($\Delta = 22.4–13.5\ cm^{-1}$) only small changes should occur for the spin projection coefficients

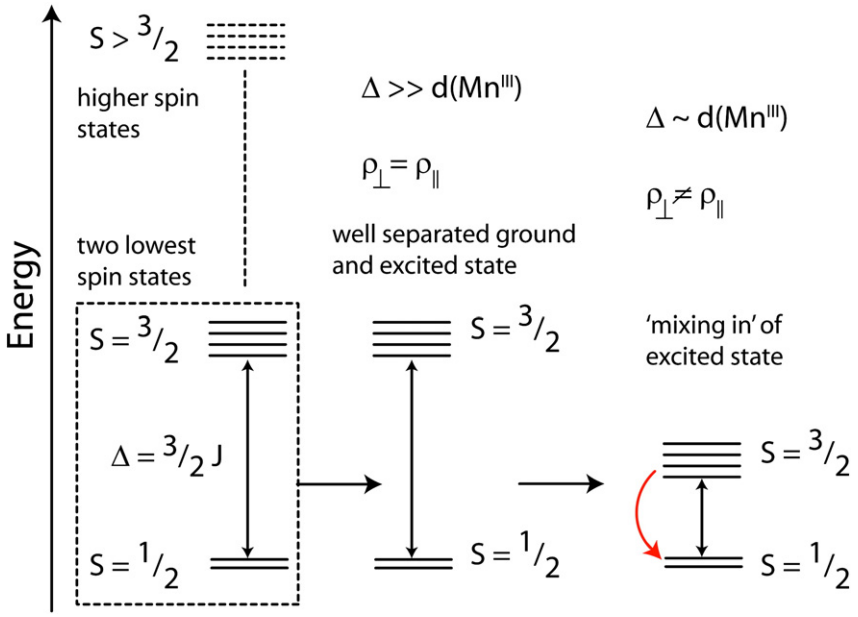

Fig. 6. The energy levels of the OEC. In the limit where energy separation between ground and first excited state (Δ) is large compared to the on-site ZFS (d) of the Mn^{III} ion, the perpendicular and parallel components of spin projection tensor ($\rho_\perp$, $\rho_{||}$) are approximately equal. In the limit where Δ is of the same magnitude as the on-site ZFS of the Mn^{III}, a large difference (anisotropy) in the perpendicular and parallel components of the spin projection tensor ($\rho_\perp$, $\rho_{||}$) is expected.

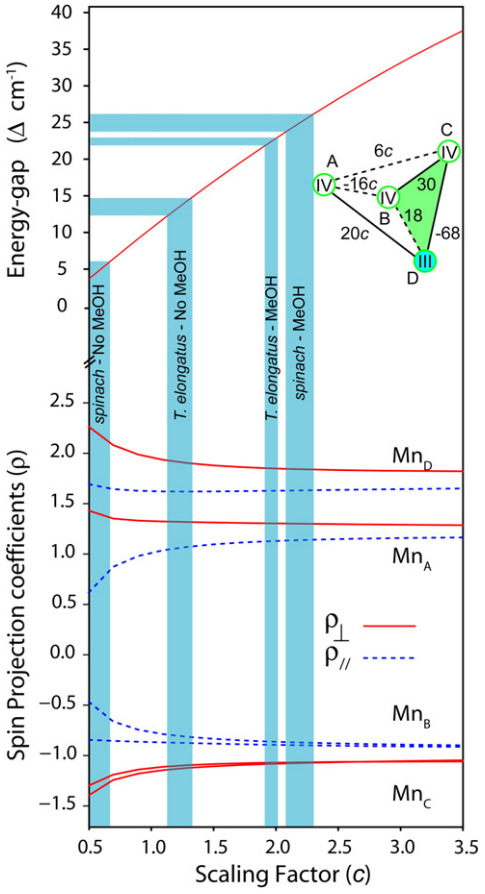

Fig. 7. Top: The dependence of the ground to first excited state energy difference on the coupling of Mn_A to the trimer unit. The extent of coupling between Mn_A and the trimer is given in terms of the factor *c*. The factor *c* is applied to all three exchange couplings that connect Mn_A to the trimer (J_{AB}, J_{AC}, J_{AD}), and thus represents an average increase/decrease in the coupling of the two OEC fragments. Bottom: The dependence of the spin projection factors ($\rho_\perp$, $\rho_{||}$) on the factor *c*, described above. The zero-field splitting parameter (*d*) of the Mn^{III} ion was fixed to the value determined in section 4.3 i.e. $d = -1.2\ cm^{-1}$. $c = 1$ gives the original Siegbahn coupling scheme.

(<10%). As such, no change in the EPR/ENDOR spectra is expected, as observed. The range of energy gap values observed for spinach is much larger ($\Delta = 25–35\ cm^{-1}$ to $2–6\ cm^{-1}$), and as a consequence a more significant change in the spin projection coefficients is expected. Importantly, the spinach PS II sample in the absence of MeOH has an energy gap of only $2–6\ cm^{-1}$. In this regime large deviations are observed for the spin projection coefficients as the spin ½ model for the ground state breaks down. Note that: $c = 1$ gives the original coupling scheme of the Siegbahn model. This gives an energy gap of $\sim 10\ cm^{-1}$, approximately that seen for *T. elongatus* without MeOH.

The above arguments bring into question the simulations of Charlot et al. [68] performed on the broad S_2 multiline signal of plant PS II in the absence of MeOH. The broad multiline signal in this earlier study refers to the component of the multiline signal that is sensitive to NIR light (see introduction). In this earlier study the multiline signal was assumed to arise from a well isolated spin ½ ground state. The above results demonstrate that this is not the case. In the absence of MeOH, the energy spacing (Δ) in spinach PS II is of the order of the on-site zero-field splitting/fine structure of the Mn^{III}. As such, it is unclear whether a spin ½ model for this system is appropriate as it does not explicitly include the Spin Hamiltonian terms that describe the on-site zero-field splitting of the Mn^{III}. In this circumstance it is expected that a more complicated two- or four-spin model should be used that does include these terms.

Table 4
Theoretical interspin distances between the methyl deuterons of the CD_3OH and Mn_A/Mn_D using the point dipole model.

		^2H (MHz)	Theoretical distance (Å)				
			Å (ρ = 1)	Mn_A-Asp170 (ρ = 1.33)	Mn_A-OH (ρ = 1.01)	Mn_D-Glu189 (ρ = 1.62)	Mn_D-open (ρ = 1.96)
a	CD_3	0.448	3.00	3.30	3.01	3.51	3.76
		0.209	3.91	4.29	3.92	4.59	4.89
		0.177	4.10	4.51	4.11	4.81	5.13
b	CD_3	0.64	2.67	2.93	2.68	3.13	3.34
		0.38	3.15	3.46	3.16	3.70	3.94
		0.38	3.15	3.46	3.16	3.70	3.94

[a]Exp. data of Force et al. [64]. [b]Exp. data of Åhrling et al. [66].

4.4. Methanol–OEC interaction in plant and cyanobacterial PS II

^{2}H-ESEEM measurements performed on the S_2 state of plant PS II demonstrated that one MeOH molecule interacts with the OEC, i.e. it coordinates one of the Mn ions [64,66]. Similar data has yet to be reported for *T. elongatus* PS II. In the studies reported in the literature, ^{2}H couplings were reported in the range of 0.2–0.6 MHz. In both studies, best fits where obtained using two inequivalent nuclei for the deuterons of the methyl group, i.e. one more strongly coupled deuteron and two approximately identical more weakly coupled deuterons. Curiously, the two reports give contradictory results; ^{2}H couplings were approximately 1.5- to 2-fold larger in the second study. We offer no assessment of which experimental data set and subsequent analysis is correct. We note though that in the second study this discrepancy was accounted for by invoking sample heterogeneity [66]. Here it was stated that in the original study of Force et al. the S_2 state was generated by low temperature illumination leading to a mixture of S_2 (multiline) states that represent both the MeOH bound and non-bound OEC. In contrast, the study of Åhrling et al. used room temperature laser flash advancement, yielding a more homogeneous S_2 state i.e. uniformly MeOH bound. As multiline heterogeneity in spinach PS II has been well documented in the literature, this explanation seems reasonable [55,90,91].

Within the Siegbahn model, there are four good Mn-ligand/residue candidates for MeOH displacement: the two Mn_A-OH ligands, the Mn_A-Asp170 ligand and the Mn_D-Glu189. Using the anisotropic spin projection values determined in the discussion section 4.2, theoretical estimates can be made for the expected MeOH bound Mn-^{2}H interspin distances (See Table 4). Here we employ the point dipole model for the Mn-^{2}H interspin distance. This should give reasonably good estimates for the Mn-^{2}H interspin distance for ligands bound to Mn_A (the 'external' Mn), and poorer estimates for the Mn of the trimer unit (Mn_B, Mn_C, Mn_D). This simple approach was used due to the uncertainty of the binding mode of the MeOH at each of the four sites identified. This forms ongoing work in our laboratory.

Each ESEEM data set, Force [64] or Åhrling [66], is consistent with one binding position using the Siegbahn model [4]. The results of Force et al. [64] favor displacement of one of the OH ligands on Mn_A. The theoretical Mn-^{2}H distances for this site match those seen for $Mn^{III}Mn^{IV}$ model complexes where MeOH is bound to the Mn^{III} [92]. In contrast, the results of Åhrling et al. [66] give very short Mn-^{2}H distances for Mn_A either displacing the OH or Asp170, outside the range seen for model complexes and as such binding at Mn_A can be excluded assuming this data set is correct. This data set instead favors binding at Mn_D displacing the Glu189. It is again reiterated though that a more complete multipole treatment of the dipolar coupling interaction is required to precisely assign the position of MeOH binding.

It is noted that MeOH could also potentially bind at the open coordination site on Mn_D. This would give reasonable values for Mn-^{2}H distances using the coupling values of Åhrling et al. [66] However, if MeOH does bind at this open site, a significant rearrangement of the core geometry is required as a MeOH molecule can otherwise not fit into this site. Indeed the site itself is too small to bind even a water molecule, as has been previously discussed in the literature [4] (Fig. 8). A structural change of the OEC of this magnitude should lead to a large change of the electronic structure that would seem inconsistent with the data presented in this manuscript and as such, this binding mode is not favored.

As stated in section 4.3, we consider that the mechanism for MeOH action is to somehow modulate the electronic coupling between Mn_A and the trimer unit (Mn_B, Mn_C, Mn_D). This action could potentially be rationalized for the two binding models, 'Force' and 'Åhrling', discussed above. In the Force model, the replacement of either of the negatively charged OH ligands around Mn_A with MeOH would affect the distribution of electron density in the OEC core, directly changing the nature of the Mn_A–Mn_B interaction. This might lead to a larger Mn_A–Mn_B anti-ferromagnetic coupling and as such, a modification of the spin ladder of the system consistent with the data presented. The species-dependent effect of MeOH could describe a change in ligand mobility. While the same ligand is likely to be substituted in either the plant or cyanobacterial OEC, the 2nd coordination sphere interaction between the MeOH and the surrounding protein pocket could differ, thus changing the binding mode of the MeOH molecule, its H-bonding interactions and thus its effect on the electronic coupling within the OEC. In an analogous way, direct substitution of the Glu189 ligand to Mn_D (Åhrling model) could also explain the change in the electronic coupling between the Mn_A and the trimer unit (Mn_B, Mn_C, Mn_D). Direct substitution of Glu189 with MeOH would have an effect similar to that of ligand substitution on Mn_A, but within the Mn_B, Mn_C, Mn_D subunit, again possibly giving rise to a stronger Mn_A–trimer exchange interaction through a propagation of the localized electron and spin density rearrangement of the trimer subunit. Here, as with direct substitution of Asp170 on Mn_A the species-dependent effect of MeOH could be rationalized in the context of the facility of protein ligand displacement being dependent on differences between the proteins from spinach and *T. elongatus* further away from the OEC core itself. Indeed differences in rigidity – or lack of rigidity – of the Glu189 amino acid within the two species could play an important role in its possible direct substitution by MeOH.

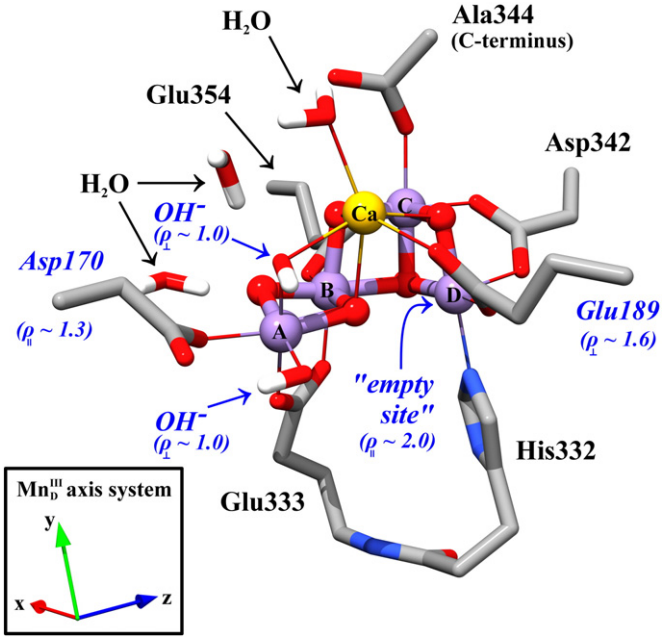

Fig. 8. Potential sites for MeOH binding for the Siegbahn model [4]. Ligands that can be substituted for MeOH and that are consistent with the ESEEM studies of either Force et al. [64] or Åhrling et al. [66] are labelled in blue italic. The Arg357 as well as backbone H-atoms are not included in the figure for clarity. The orientation of the spin projection coefficients is defined by the axis system of the Mn^{III} ion shown in the inset.

4.5. Structural flexibility of the Mn_4O_xCa cluster

S_n state dependent structural changes were proposed both from biochemical and spectroscopic studies of the OEC. A structural rearrangement during the $S_2 \rightarrow S_3$ transition was demonstrated by Boussac et al. [93,94] and Messinger et al. [95]. Here it was shown that: (i) the protein has a lower affinity for Ca in S_3; (ii) that the S_3 state has a much slower reactivity towards NH_2OH and NH_2NH_2; and (iii) a slower rate of NH_3 binding in S_3. Similarly, temperature

dependent measurements of the reduction kinetics of Y_Z^{ox} provided evidence for a high reorganization energy for the $S_2 \rightarrow S_3$ transition [96,97]. Subsequently, EXAFS measurements [98–103] provided strong spectroscopic evidence for structural changes during the $S_2 \rightarrow S_3$, and also the S_0–S_1 transitions, and also FTIR experiments [104,105] suggest significant alterations in carboxylic acid vibrations during the $S_2 \rightarrow S_3$ transition. It can therefore be proposed that the structural flexibility of the Mn_4O_xCa cluster is a key feature for its high water-oxidation rates [2,3,103,106]. This hypothesis is supported by the recent work of Siegbahn on modeling the reaction pathway for water-splitting [4] (for similar proposals see also [2,69,107]). The facility for structural rearrangement has been identified as a key feature in this theoretical water-splitting pathway. Without this flexibility the OEC would not be able to oxidize water. Similarly, structural flexibility within a given oxidation state (S_n state) of the Mn_4O_xCa cluster has been proposed based on mechanistic considerations, EPR simulations and DFT calculations [32,34,106]. It should be noted that the effect of these rearrangements, in the context of this work, would be to alter the coupling between the Mn centers, changing the effective spin ladder. Upon the addition of MeOH, one conformation, or possibly a subset of conformations, is stabilized over the remaining conformations, giving rise to the homogeneous multiline signal observed.

Conclusion

The electronic properties of the Mn_4O_xCa cluster in the S_2 state of the OEC of the thermophilic cyanobacterium *T. elongatus* and higher plants (spinach) were shown to be very similar. The data presented here show that both OEC types can be explained using the same electronic coupling scheme, namely a coupling scheme based on the structural model of Siegbahn [4,36]. The small spectral changes observed between the two species are interpreted within a model in which the contribution of the on-site ZFS of the only Mn^{III} of the S_2 to the total ZFS of the cluster changes. An analogous argument is invoked to explain the spectral differences seen in the presence and absence of MeOH. Potential sites for MeOH binding are discussed within the context of the Siegbahn model, which are consistent with the earlier ESEEM studies of Force et al. [64] and Åhrling et al. [66].

Acknowledgment

Financial supported was provided by the DFG (Me1629/2-4), the Max Planck Gesellschaft, the EU SOLAR-H2 (FP7 contract 212508), the Wallenberg and Kempe foundations and VR (J.M.), National Natural Science Foundation of China (31070211) and Initial Funding of University of Science and Technology of China (ZC9850290071) (J.S.). L.R. is a fellow of North Rhine-Westphalia (NRW) Research School BioStruct program.

References

[1] W. Lubitz, E.J. Reijerse, J. Messinger, Solar water-splitting into H_2 and O_2: design principles of photosystem II and hydrogenases, Energy Environ. Sci. 1 (2008) 15–31.
[2] J. Messinger, G. Renger, Photosynthetic water splitting, in: G. Renger (Ed.), Primary processes of photosynthesis—part 2: basic principles and apparatus, Royal Society of Chemistry, Cambridge, 2008, pp. 291–349.
[3] W. Hillier, J. Messinger, Mechanism of photosynthetic oxygen production, Springer, 2005.
[4] P.E.M. Siegbahn, Structures and energetics for O2 formation in photosystem II, Acc. Chem. Res. 42 (2009) 1871–1880.
[5] H. Dau, I. Zaharieva, Principles, efficiency, and blueprint character of solar-energy conversion in photosynthetic water oxidation, Accounts Chem. Res. 42 (2009) 1861–1870.
[6] J.P. McEvoy, G.W. Brudvig, Water-splitting chemistry of photosystem II, Chem. Rev. 106 (2006) 4455–4483.
[7] K. Åhrling, R.J. Pace, M.C.W. Evans, The catalytic manganese cluster: implications from spectroscopy, Springer, 2005.
[8] N. Nelson, C.F. Yocum, Structure and function of photosystems I and II, Annu. Rev. Plant Biol. 57 (2006) 521–565.
[9] G. Renger, T. Renger, Photosystem II: the machinery of photosynthetic water splitting, Photosynth. Res. 98 (2008) 53–80.
[10] J. Yano, J. Kern, K. Sauer, M.J. Latimer, Y. Pushkar, J. Biesiadka, B. Loll, W. Saenger, J. Messinger, A. Zouni, V.K. Yachandra, Where water is oxidized to dioxygen: structure of the photosynthetic Mn4Ca cluster, Science 314 (2006) 821–825.
[11] B. Kok, B. Forbush, M. McGloin, Cooperation of charges in photosynthetic O_2 evolution-1. A linear four step mechanism, Photochem. Photobiol. 11 (1970).
[12] M. Haumann, P. Liebisch, C. Müller, M. Barra, M. Grabolle, H. Dau, Photosynthetic O_2 formation tracked by time-resolved X-ray experiments, Science 310 (2005) 1019–1021.
[13] H. Dau, A. Grundmeier, P. Loja, M. Haumann, On the structure of the manganese complex of photosystem II: extended-range EXAFS data and specific atomic-resolution models for the four S-states, Phil. Trans. R. Soc. B 363 (2008) 1237–1244.
[14] J. Clausen, W. Junge, Detection of an intermediate of photosynthetic water oxidation, Nature 430 (2004) 480–483.
[15] D.R.J. Kolling, T.S. Brown, G. Ananyev, G.C. Dismukes, Photosynthetic oxygen evolution is not reversed at high oxygen pressures: mechanistic consequences for the water-oxidizing complex, Biochemistry 48 (2009).
[16] D. Shevela, K. Beckmann, C. Clausen, W. Junge, J. Messinger, Membrane-inlet-mass spectrometry reveals a high driving force for oxygen-production by photosystem II, Proc. Natl. Acad. Sci. USA 108 (9) (2011) 3602–3607.
[17] S. Styring, A.W. Rutherford, In the oxygen-evolving complex of photosystem II the S_0 state is oxidized to the S_1 state by D^+ (signal II_{slow}), Biochemistry 26 (1987) 2401–2405.
[18] W.F.J. Vermaas, G. Renger, G. Dohnt, The reduction of the oxygen-evolving system in chloroplasts by thylakoid components, Biochim. Biophys. Acta 764 (1984) 194–202.
[19] A. Zouni, H.T. Witt, J. Kern, P. Fromme, N. Krauss, W. Saenger, P. Orth, Crystal structure of photosystem II from Synechococcus elongatus at 3.8 Ångstrom resolution, Nature 409 (2001) 739–743.
[20] N. Kamiya, J.R. Shen, Crystal structure of oxygen-evolving photosystem II from Thermosynechococcus vulcanus at 3.7-Ångstrom resolution, Proc. Natl. Acad. Sci. USA 100 (2003) 98–103.
[21] K.N. Ferreira, T.M. Iverson, K. Maghlaoui, J. Barber, S. Iwata, Architecture of the photosynthetic oxygen-evolving center, Science 303 (2004) 1831–1838.
[22] A. Guskov, A. Gabdulkhakov, M. Broser, C. Glöckner, J. Hellmich, J. Kern, J. Frank, F. Müh, W. Saenger, A. Zouni, Recent progress in the crystallographic studies of photosystem II, ChemPhysChem 11 (2010) 1160–1171.
[23] B. Loll, J. Kern, W. Saenger, A. Zouni, J. Biesiadka, Towards complete cofactor arrangement in the 3.0 Å resolution structure of photosystem II, Nature 438 (2005) 1040–1044.
[24] A new crystal structure was recently disclosed by Jian-Ren Shen (Okayama University, Japan) at the 15th International Congress of Photosynthesis. This new structure has yet to be published and as such, is not explicitly considered in this manuscript. It is noted that the structure of the OEC reported is most similar to the Siegbahn structure.
[25] A. Guskov, J. Kern, A. Gabdulkhakov, M. Broser, A. Zouni, W. Saenger, Cyanobacterial photosystem II at 2.9-A resolution and the role of quinones, lipids, channels and chloride, Nat. Struct. Mol. Biol. 16 (2009) 334–342.
[26] J. Kargul, K. Maghlaoul, J.W. Murray, Z. Deak, A. Boussac, A.W. Rutherford, I. Vass, J. Barber, Purification, crystallization and X-ray diffraction analyses of the *T. elongatus* PSII core dimer with strontium replacing calcium in the oxygen-evolving complex, Biochim. Biophys. Acta 1767 (2007) 404–413.
[27] Y. Pushkar, J. Yano, P. Glatzel, J. Messinger, A. Lewis, K. Sauer, U. Bergmann, V.K. Yachandra, Structure and orientation of the Mn_4Ca cluster in plant photosystem II membranes studied by polarized range-extended x-ray absorption spectroscopy, J. Biol. Chem. 282 (2007) 7198–7208.
[28] R.M. Cinco, J.H. Robblee, J. Messinger, C. Fernandez, K.L.M. Holman, K. Sauer, V.K. Yachandra, Orientation of calcium in the Mn_4O_XCa of the oxygen-evolving complex determined using polarized strontium EXAFS of photosystem II membranes, Biochemistry 43 (2004) 13271–13282.
[29] E.M. Sproviero, J.A. Gascón, J.P. McEvoy, G.W. Brudvig, V.S. Batista, QM/MM models of the O2-evolving complex of photosystem II, J. Chem. Theory Comput. 2 (2006) 1119–1134.
[30] E.M. Sproviero, J.A. Gascón, J.P. McEvoy, G.W. Brudvig, V.S. Batista, A model of the oxygen-evolving center of photosystem II predicted by Structural refinement based on EXAFS simulations, J. Am. Chem. Soc. 130 (2008) 6728–6730.
[31] E.M. Sproviero, J.A. Gascón, J.P. McEvoy, G.W. Brudvig, V.S. Batista, Quantum mechanics/molecular mechanics structural models of the oxygen-evolving complex of photosystem II, Curr. Opin. Struct. Biol. 17 (2007) 173–180.
[32] S. Petrie, R. Stranger, P. Gatt, Ron J. Pace, Bridge over troubled water: resolving the competing photosystem II crystal structures, Chem. Eur. J. 13 (2007) 5082–5089.
[33] S. Petrie, R. Stranger, R.J. Pace, Structural, magnetic coupling and oxidation state trends in models of the $CaMn_4$ cluster in photosystem II, Chem. Eur. J. 14 (2008) 5482–5494.
[34] M. Kusunoki, Mono-manganese mechanism of the photosystem II water splitting reaction by a unique Mn_4Ca cluster, Biochim. Biophys. Acta 1767 (2007) 484–492.
[35] H. Dau, M. Haumann, The manganese complex of photosystem II in its reaction cycle—basic framework and possible realization at the atomic level, Coord. Chem. Rev. 252 (2008) 273–295.
[36] D.A. Pantazis, M. Orio, T. Petrenko, S. Zein, W. Lubitz, J. Messinger, F. Neese, Structure of the oxygen-evolving complex of photosystem II: information on the S_2 state through quantum chemical calculation of its magnetic properties, Phys. Chem. Chem. Phys. 11 (2009) 6788–6798.

[37] P.E.M. Siegbahn, A structure-consistent mechanism for dioxygen formation in photosystem II, Chem. Eur. J. 14 (2008) 8290–8302.
[38] P.E.M. Siegbahn, An energetic comparison of different models for the oxygen evolving complex of photosystem II, J. Am. Chem. Soc. 131 (2009) 18238–18239.
[39] N. Cox, L. Rapatskiy, J.-H. Su, D.A. Pantazis, M. Sugiura, L. Kulik, P. Dorlet, A.W. Rutherford, F. Neese, A. Boussac, W. Lubitz, J. Messinger, The effect of Ca^{2+}/Sr^{2+} substitution on the electronic structure of the oxygen-evolving complex of photosystem II: a combined multi-frequency EPR, ^{55}Mn-ENDOR and DFT study of the S_2 state, J. Am. Chem. Soc. 133 (10) (2011) 3635–3648.
[40] G.C. Dismukes, Y. Siderer, Intermediates of a polynuclear manganese center involved in photosynthetic oxidation of water, Proc. Natl. Acad. Sci. USA 78 (1981) 274–278.
[41] H. Levanon, K. Möbius, Advanced EPR spectroscopy on electron transfer processes in photosynthesis and biomimetic model systems, Annu. Rev. Biophys. Biomol. 26 (1997) 495–540.
[42] R.D. Britt, J.M. Peloquin, K.A. Campbell, Pulsed and parallel-polarization EPR characterization of the photosystem II oxygen-evolving complex, Annu. Rev. Biophys. Biomol. 29 (2000) 463–495.
[43] A. Haddy, EPR spectroscopy of the manganese cluster of photosystem II, Photosynth. Res. 92 (2007) 357–368.
[44] K.A. Campbell, D.A. Force, P.J. Nixon, F. Dole, B.A. Diner, R.D. Britt, Dual-mode EPR detects the initial intermediate in photoassembly of the photosystem II Mn cluster: the influence of amino acid residue 170 of the D1 polypeptide on Mn coordination, J. Am. Chem. Soc. 122 (2000) 3754–3761.
[45] S.L. Dexhemier, M.P. Klein, Detection of a paramagnetic intermediate in the S_1 state of the photosynthetic oxygen-evolving complex, J. Am. Chem. Soc. 114 (1992) 2821–2826.
[46] T. Yamauchi, H. Mino, T. Matsukawa, A. Kawamori, T. Ono, Parallel polarization electron paramagnetic resonance studies of the S_1-state manganese cluster in the photosynthetic oxygen-evolving system, Biochemistry 36 (1997) 7520–7526.
[47] A. Boussac, M. Sugiura, A.W. Rutherford, P. Dorlet, Complete EPR spectrum of the S_3-state of the oxygen-evolving photosystem II, J. Am. Chem. Soc. 131 (2009) 5050.
[48] K.A. Åhrling, S. Peterson, S. Styring, The S_0 state EPR signal from the Mn cluster in photosystem II arises from an isolated $S = 1/2$ ground state, Biochemistry 37 (1998) 8115–8120.
[49] J. Messinger, J.H.A. Nugent, M.C.W. Evans, Detection of an EPR multiline signal for the S_0^* state in photosystem II, Biochemistry 36 (1997) 11055–11060.
[50] J. Messinger, J.H. Robblee, W.O. Yu, K. Sauer, V.K. Yachandra, M.P. Klein, The S_0 state of the oxygen-evolving complex in photosystem II is paramagnetic: detection of an EPR multiline signal, J. Am. Chem. Soc. 119 (1997) 11349–11350.
[51] O. Horner, E. Rivière, G. Blondin, S. Un, A.W. Rutherford, J.-J. Girerd, A. Boussac SQUID Magnetization Study of the Infrared-Induced Spin Transition in the S_2 State of Photosystem II: Spin Value Associated with the $g = 4.1$ EPR Signal, J. Am. Chem. Soc. 120 (1998) 7924–7928.
[52] A. Boussac, A.W. Rutherford, Comparative study of the $g = 4.1$ EPR signals in the S_2-state of photosystem II. Biochim. Biophys. Acta 1457 (2000) 145–156.
[53] A. Boussac, J.J. Girerd, A.W. Rutherford, Conversion of the spin state of the manganese complex in photosystem II induced by near-infrared light, Biochemistry 35 (1996) 6984–6989.
[54] R.J. Pace, P.J. Smith, R. Bramley, D. Stehlik, EPR saturation and temperature dependence studies on signals from the oxygen-evolving centre of photosystem II, Biochim. Biophys. Acta 1058 (1991) 161–170.
[55] A. Boussac, Inhomogeneity of the EPR multiline signal from the S_2-state of the photosystem II oxygen evolving enzyme, J. Biol. Inorg. Chem. 2 (1997) 580–585.
[56] P. Geijer, S. Peterson, K.A. Åhrling, Z. Deak, S. Styring, Comparative studies of the S_0 and S_2 multiline electron paramagnetic resonance signals from the manganese cluster in photosystem II, Biochim. Biophys. Acta 1503 (2001) 83–95.
[57] Z. Deak, S. Peterson, P. Geijer, K.A. Åhrling, S. Styring, Methanol modification of the electron paramagnetic resonance signals from the S_0 and S_2 states of the water-oxidizing complex of photosystem II, Biochim. Biophys. Acta 1412 (1999) 240–249.
[58] K.A. Åhrling, S. Peterson, S. Styring, An oscillating manganese electron paramagnetic resonance signal from the S_0 state of the oxygen evolving complex in photosystem II, Biochemistry 36 (1997) 13148–13152.
[59] T. Matsukawa, H. Mino, D. Yoneda, A. Kawamori, Dual-mode EPR study of new signals from the S_3-state of oxygen-evolving complex in photosystem II, Biochemistry 38 (1999) 4072–4077.
[60] J.H. Su, K.G.V. Havelius, F. Mamedov, F.M. Ho, S. Styring, Split EPR signals from photosystem II are modified by methanol, reflecting S state-dependent binding and alterations in the magnetic coupling in the $CaMn_4$ cluster, Biochemistry 45 (2006) 7617–7627.
[61] N. Cox, F.M. Ho, N. Pewnim, R. Steffen, P.J. Smith, K.G.V. Havelius, J.L. Hughes, L. Debono, S. Styring, E. Krausz, R.J. Pace, The S_1 split signal of photosystem II; a tyrosine-manganese coupled interaction, Biochim. Biophys. Acta 1787 (2009) 882–889.
[62] A. Boussac, H. Kuhl, S. Un, M. Rögner, A.W. Rutherford, Effect of near-infrared light on the S_2-state of the manganese complex of photosystem II from *Synechococcus elongatus*, Biochemistry 37 (1998) 8995–9000.
[63] A. Boussac, H. Kuhl, E. Ghibaudi, M. Rögner, A.W. Rutherford, Detection of an electron paramagnetic resonance signal in the S_0 state of the manganese complex of photosystem II from *Synechococcus elongatus*, Biochemistry 38 (1999) 11942–11948.
[64] D.A. Force, D.W. Randall, G.A. Lorigan, K.L. Clemens, R.D. Britt, ESEEM studies of alcohol binding to the manganese cluster of the oxygen evolving cluster of photosystem II, J. Am. Chem. Soc. 120 (1998) 13321–13333.
[65] R.D. Britt, K.A. Campbell, J.M. Peloquin, M.L. Gilchrist, C.P. Aznar, M.M. Dicus, J. Robblee, J. Messinger, Recent pulsed EPR studies of the photosystem II oxygen-evolving complex: implications as to water oxidation mechanisms, Biochim. Biophys. Acta 1655 (2004) 158–171.
[66] K.A. Åhrling, M.C.W. Evans, J.H.A. Nugent, R.J. Ball, R.J. Pace, ESEEM studies of substrate water and small alcohol binding to the oxygen-evolving complex of photosystem II during functional turnover, Biochemistry 45 (2006) 7069–7082.
[67] B. Nöring, D. Shevela, G. Renger, J. Messinger, Effects of methanol on the S_i-state transitions in photosynthetic water-splitting, Photosynth. Res. 98 (2008) 251–260.
[68] M.-F. Charlot, A. Boussac, G. Blondin, Towards a spin coupling model for the Mn_4 cluster in photosystem II, Biochim. Biophys. Acta 1708 (2005) 120–132.
[69] L.V. Kulik, B. Epel, W. Lubitz, J. Messinger, Electronic structure of the Mn_4O_xCa cluster in the S_0 and S_2 states of the oxygen-evolving complex of photosystem II based on pulse ^{55}Mn ENDOR and EPR Spectroscopy, J. Am. Chem. Soc. 129 (2007) 13421–13435.
[70] J.M. Peloquin, K.A. Campbell, D.W. Randall, M.A. Evanchik, V.L. Pecoraro, W.H. Armstrong, R.D. Britt, ^{55}Mn ENDOR of the S_2-state multiline EPR signal of photosystem II: implications on the structure of the tetranuclear Mn cluster, J. Am. Chem. Soc. 122 (2000) 10926–10942.
[71] D.A. Berthold, G.T. Babcock, C.F. Yocum, A highly resolved, oxygen-evolving photosystem-II preparation from spinach thylakoid membranes—electron-paramagnetic-res and electron-transport properties, FEBS Lett. 134 (1981) 231–234.
[72] M. Sugiura, A. Boussac, T. Noguchi, F. Rappaport, Influence of histidine-198 of the D1 subunit on the properties of the primary electron donor, P680, of photosystem II in *Thermosynechococcus elongatus*, Biochim. Biophys. Acta 1777 (2008) 331–342.
[73] A. Boussac, F. Rappaport, P. Carrier, J.M. Verbavatz, R. Gobin, D. Kirilovsky, A.W. Rutherford, M. Sugiura, Biosynthetic Ca^{2+}/Sr^{2+} exchange in the photosystem II oxygen-evolving enzyme of Thermosynechococcus elongatus, J. Biol. Chem. 279 (2004) 22809–22819.
[74] N. Ishida, M. Sugiura, F. Rappaport, T.L. Lai, A.W. Rutherford, A. Boussac, Biosynthetic exchange of bromide for chloride and strontium for calcium in the photosystem II oxygen-evolving enzymes, J. Biol. Chem. 283 (2008) 13330–13340.
[75] L. Kulik, B. Epel, J. Messinger, W. Lubitz, Pulse EPR, ^{55}Mn ENDOR and ELDOR-detected NMR of the S_2-state of the oxygen evolving complex in photosystem II, Photosynth. Res. 84 (2005) 347–353.
[76] L.V. Kulik, B. Epel, W. Lubitz, J. Messinger, ^{55}Mn pulse ENDOR at 34 GHz of the S_0 and S_2 states of the oxygen-evolving complex in photosystem II, J. Am. Chem. Soc. 127 (2005) 2392–2393.
[77] B. Epel, I. Gromov, S. Stoll, A. Schweiger, D. Goldfarb, Spectrometer manager: a versatile control software for pulse EPR spectrometers, Concepts Magn. Res. B 26B (2005) 36–45.
[78] C. Teutloff, S. Kessen, J. Kern, A. Zouni, R. Bittl, High-field (94-GHz) EPR spectroscopy on the S_2 multiline signal of photosystem II, FEBS Lett. 580 (2006) 3605–3609.
[79] D.W. Randall, B.E. Sturgeon, J.A. Ball, G.A. Lorigan, M.K. Chan, M.P. Klein, W.H. Armstrong, R.D. Britt, ^{55}Mn ESE-ENDOR of a mixed valence Mn(III)Mn(IV) complex: comparison with the Mn cluster of the photosynthetic oxygen-evolving complex, J. Am. Chem. Soc. 117 (1995) 11780–11789.
[80] K.O. Schäfer, R. Bittl, W. Zweygart, F. Lendzian, G. Haselhorst, T. Weyhermüller, K. Wieghardt, W. Lubitz, Electronic structure of antiferromagnetically coupled dinuclear manganese ($Mn^{III}Mn^{IV}$) complexes studied by magnetic resonance techniques, J. Am. Chem. Soc. 120 (1998) 13104–13120.
[81] M. Zheng, G.C. Dismukes, Orbital configuration of the valence electrons, ligand field symmetry, and manganese oxidation states of the photosynthetic water oxidizing complex: analysis of the S_2 state multiline EPR signals, Inorg. Chem. 35 (1996) 3307–3319.
[82] M. Zheng, S.V. Khangulov, G.C. Dismukes, V.V. Barynin, Electronic structure of dimanganese(II, III) and dimanganese(III, IV) complexes and dimanganese catalase enzyme: a general EPR spectral simulation approach, Inorg. Chem. 33 (1994) 382–387.
[83] R. Orbach, Spin-lattice relaxation in rare-earth salts, Proc. R. Soc. Lon. Ser-A 264 (1961) 458–484.
[84] A. Schweiger, G. Jeschke, Princples of pulse electron paramagnetic resonance, Oxford University Press, Oxford, 2001.
[85] G.A. Lorigan, R.D. Britt, Temperature-dependent pulsed electron-paramagnetic-resonance studies of the S_2 state multiline signal of the photosynthetic oxygen-evolving complex, Biochemistry 33 (1994) 12072–12076.
[86] J.W. Murray, J. Barber, Structural characteristics of channels and pathways in photosystem II including the identification of an oxygen channel, 3rd International Conference on Structure, Dynamics and Function of Proteins in Biological Membranes, vol. 159, J. Struc. Biol., Mt Verita, Switzerland, 2006, pp. 228–237.
[87] F.M. Ho, S. Styring, Access channels and methanol binding site to the $CaMn_4$ cluster in photosystem II based on solvent accessibility simulations, with implications for substrate water access, Biochim. Biophys. Acta 1777 (2008) 140–153.
[88] R.J. Debus, Protein ligation of the photosynthetic oxygen-evolving center, Coord. Chem. Rev. 252 (2008) 244–258.
[89] M. Sugiura, F. Rappaport, W. Hillier, P. Dorlet, Y. Ohno, H. Hayashi, A. Boussac, Evidence that D1-His332 in photosystem II from Thermosynechococcus elongatus Interacts with the S_3-state and not with the S_2-state, Biochemistry 48 (2009) 7856–7866.
[90] A. Boussac, J.-J. Girerd, A. Rutherford, Conversion of the spin state of the manganese cluster in photosystem II induced by near-infrared light, Biochemistry 35 (1996) 6984–6989.

[91] K.A. Åhrling, M.C.W. Evans, J.H.A. Nugent, R.J. Pace, The two forms of the S_2 state multiline signal in photosystem II: effect of methanol and ethanol, Biochim. Biophys. Acta 1656 (2004) 66–77.
[92] D.W. Randall, A. Gelasco, M.T. Caudle, V.L. Pecoraro, R.D. Britt, ESE-ENDOR and ESEEM characterization of water and methanol ligation to a dinuclear Mn(III)Mn (IV) complex, J. Am. Chem. Soc. 119 (1997) 4481–4491.
[93] A. Boussac, A.W. Rutherford, Ca^{2+} binding to the oxygen evolving enzyme varies with the redox state of the Mn cluster, FEBS Lett. 236 (1988) 432–436.
[94] A. Boussac, A.W. Rutherford, S. Styring, Interaction of ammonia with the water splitting enzyme of photosystem II, Biochemistry 29 (1990) 24–32.
[95] J. Messinger, U. Wacker, G. Renger, Unusual low reactivity of the water oxidase in redox state S_3 toward exogenous reductants. Analysis of the NH_2OH- and NH_2NH_2-induced modifications of flash-induced oxygen evolution in isolated spinach thylakoids, Biochemistry 30 (1991) 7852–7862.
[96] H. Koike, B. Hanssum, Y. Inoue, G. Renger, Temperature dependence of S-state transition in a thermophilic cyanobacterium, Synechococcus vulcanus Copeland measured by absorption changes in the ultraviolet region, Biochim. Biophys. Acta 893 (1987) 524–533.
[97] G. Renger, B. Hanssum, Studies on the reaction coordinates of the water oxidase in PS II membrane fragments from spinach, FEBS Lett. 299 (1992) 28–32.
[98] R.D. Guiles, J.L. Zimmermann, A.E. McDermott, V.K. Yachandra, J.L. Cole, S.L. Dexheimer, R.D. Britt, K. Wieghardt, U. Bossek, The S_3 state of photosystem II: differences between the structure of the manganese complex in the S_2 and S_3 states determined by x-ray absorption spectroscopy, Biochemistry-Us 29 (1990) 471–485.
[99] W. Liang, T.A. Roelofs, R.M. Cinco, A. Rompel, M.J. Latimer, W.O. Yu, K. Sauer, M.P. Klein, V.K. Yachandra, Structural change of the Mn cluster during the $S_2 \rightarrow S_3$ state transition of the oxygen-evolving complex of photosystem II. Does it reflect the onset of water/substrate oxidation? Determination by Mn X-ray absorption spectroscopy, J. Am. Chem. Soc. 122 (2000) 3399–3412.
[100] H. Dau, L. Iuzzolino, J. Dittmer, The tetra-manganese complex of photosystem II during its redox cycle—X-ray absorption results and mechanistic implications, Biochim. Biophys. Acta 1503 (2001) 24–39.
[101] J.H. Robblee, J. Messinger, R.M. Cinco, K.L. McFarlane, C. Fernandez, S.A. Pizarro, K. Sauer, V.K. Yachandra, The Mn cluster in the S_0 state of the oxygen-evolving complex of photosystem II studied by EXAFS spectroscopy: are there three di-μ-oxo-bridged Mn_2 moieties in the tetranuclear Mn complex? J. Am. Chem. Soc. 124 (2002) 7459–7471.
[102] M. Haumann, C. Müller, P. Liebisch, L. Iuzzolino, J. Dittmer, M. Grabolle, T. Neisius, W. Meyer-Klaucke, H. Dau, Structural and oxidation state changes of the photosystem II manganese complex in four transitions of the water oxidation cycle ($S_0 \rightarrow S_1$, $S_1 \rightarrow S_2$, $S_2 \rightarrow S_3$, and $S_3 \rightarrow S_0$) characterized by x-ray absorption spectroscopy at 20 K and room temperature, Biochemistry 44 (2005) 1894–1908.
[103] Y.L. Pushkar, J. Yano, K. Sauer, A. Boussac, V.K. Yachandra, Structural changes in the Mn_4Ca cluster and the mechanism of photosynthetic water splitting, Proc. Natl. Acad. Sci. USA 105 (2008) 1879–1884.
[104] W. Hillier, G.T. Babcock, S-state dependent fourier transform infrared difference spectra for the photosystem II oxygen evolving complex, Biochemistry 40 (2001) 1503–1509.
[105] T. Noguchi, M. Sugiura, Flash-induced fourier transform infrared detection of the structural changes during the S-state cycle of the oxygen-evolving complex in photosystem II, Biochemistry 40 (2001) 1497–1502.
[106] G. Renger, Coupling of electron and proton transfer in oxidative water cleavage in photosynthesis, Biochim. Biophys. Acta 1655 (2004) 195–204.
[107] J. Messinger, Evaluation of different mechanistic proposals for water oxidation in photosynthesis on the basis of Mn_4O_xCa structures for the catalytic site and spectroscopic data, Phys. Chem. Chem. Phys. 6 (2004) 4764–4771.
[108] S. Pudollek, F. Lendzian, R. Bittl, ^{55}Mn-ENDOR of the S_2-state multiline signal of Photosystem II from Thermosynechococcus elongatus, Biochem. Soc. Trans. 36 (2008) 1001–1004.
[109] C. Teutloff, S. Pudollek, S. Keßen, M. Broser, A. Zouni, R. Bittl, Electronic structure of the tyrosine D radical and the water-splitting complex from pulsed ENDOR spectroscopy on photosystem II single crystals, Phys. Chem. Chem. Phys. 11 (2009) 6715–6726.